

Wind Forcing Controls on Antarctic Bottom Water Export From the Weddell Sea via Bottom Boundary Layer Processes

**Key Points:**

- Increased zonal wind stress and wind stress curl along steep bathymetry leads to a reduction in interannual northward AABW transport
- Speed of abyssal boundary current transporting AABW responds rapidly to changes in wind forcing via barotropic dynamics
- Barotropic acceleration of boundary current induces strengthening of downslope bottom Ekman flow, which reduces AABW thickness and transport

Supporting Information:

Supporting Information may be found in the online version of this article.

Correspondence to:

C. D. J. Auckland,
chrauc39@bas.ac.uk

Citation:

Auckland, C. D. J., Abrahamsen, E. P., Meredith, M. P., Garabato, A. C. N., Spingys, C. P., Frajka-Williams, E., & Gordon, A. L. (2024). Wind forcing controls on Antarctic Bottom Water export from the Weddell Sea via bottom boundary layer processes. *Journal of Geophysical Research: Oceans*, 129, e2024JC021089. <https://doi.org/10.1029/2024JC021089>

Received 7 MAR 2024

Accepted 27 JUL 2024

Author Contributions:

Conceptualization: C. D. J. Auckland, E. P. Abrahamsen, M. P. Meredith, A. C. Naveira Garabato, C. P. Spingys, E. Frajka-Williams

Data curation: E. P. Abrahamsen, A. L. Gordon

Formal analysis: C. D. J. Auckland

Funding acquisition: E. P. Abrahamsen, M. P. Meredith, A. C. Naveira Garabato, E. Frajka-Williams, A. L. Gordon

Investigation: C. D. J. Auckland

Methodology: C. D. J. Auckland, E. P. Abrahamsen, M. P. Meredith, A. C. Naveira Garabato, C. P. Spingys, E. Frajka-Williams

© 2024. The Author(s).

This is an open access article under the terms of the [Creative Commons Attribution License](https://creativecommons.org/licenses/by/4.0/), which permits use, distribution and reproduction in any medium, provided the original work is properly cited.

C. D. J. Auckland^{1,2} , E. P. Abrahamsen¹ , M. P. Meredith¹ , A. C. Naveira Garabato² , C. P. Spingys³ , E. Frajka-Williams⁴ , and A. L. Gordon⁵ 

¹British Antarctic Survey, Cambridge, UK, ²University of Southampton, Southampton, UK, ³National Oceanography Centre, Southampton, UK, ⁴University of Hamburg, Hamburg, Germany, ⁵Lamont-Doherty Earth Observatory, Columbia University, Palisades, NY, USA

Abstract The Antarctic Bottom Water (AABW) exported from the Weddell Sea has experienced warming and contraction in the past 30 yrs. Superposed on this decadal trend is substantial annual and interannual variability in the volume and properties of Weddell-sourced AABW. Several mechanisms have been suggested to explain these variations, many of which highlight a role of wind stress, but the comparative importance and possible simultaneity of the different mechanisms remains unclear. Using data from two mooring sites within the Weddell Sea, we find a rapid intensification of the abyssal boundary current carrying AABW through Orkney Passage (OP), the most direct export pathway of AABW from the Weddell Sea, in response to periods of strong zonal wind stress and anomalous wind stress curl along the South Scotia Ridge upstream of OP. This acceleration is concomitant with a 40% reduction in northward AABW transport in late 2015. The changes in transport follow anomalous wind forcing by approximately 3 months, with the short timescale indicative of a barotropic response in the flow through OP. The bottom boundary layer over the OP's sloping topography is found to have a key role in regulating export on monthly to interannual timescales. Increased boundary current velocity leading up to the passage forms a thickened bottom boundary layer, resulting in reduced AABW thickness and density, and thus restricting northward transport of AABW through the passage. Whilst other processes are likely to dominate on longer (decadal) periods, the dynamics identified here can explain significant variability on timescales up to interannual.

Plain Language Summary Antarctic Bottom Water (AABW) is the coldest, densest water mass in the World Ocean, and plays a pivotal role in controlling the ocean's ability to store and capture heat and carbon from the atmosphere. The volume of AABW has both warmed and shrunk over the past decades, with significant variability on shorter timescales from a few months to several years. Different mechanisms have been suggestively linked to these changes; however, their relative importance remains unclear. Here, we use observational data from two moorings along the flow path of AABW from the Weddell Sea to the South Atlantic, to investigate changes in AABW properties and volume transport. Comparing temperatures at each mooring, we find a rapid acceleration of this current is driven by stronger winds across the region. This acceleration causes a warming and reduction in transport of AABW as lighter warmer waters are pushed deeper along the seabed creating a thick turbulent and unstable layer. On longer timescales, the relationship between winds and variations in AABW transport cannot be unambiguously attributed to this mechanism, as other processes could have comparable or greater impact on the transport of AABW, however the process identified here has strong relevance on shorter timescales.

1. Introduction

Antarctic Bottom Water (AABW) is the densest oceanic water mass, and forms the deepest limb of the global overturning circulation (Johnson, 2008; Jullion et al., 2014; Orsi et al., 1999; Van Sebille et al., 2013). AABW covers much of the global abyssal ocean and accounts for the majority of waters below 4,000 m in the Pacific, Indian, and South Atlantic oceans (Purkey & Johnson, 2010). Due to the formation mechanisms and large volume of AABW, it has a pivotal role in regulating oceanic oxygen, heat, and carbon uptake (Rintoul et al., 2001). AABW has four distinct formation regions, with the largest volume exported from the Weddell Sea (Foster & Carmack, 1976; Naveira Garabato et al., 2014; Ohshima et al., 2013; Orsi et al., 1999). The Weddell Sea accounts for over half the global northward transport of AABW, as a result of both significant formation in the region and entrainment of AABW from other source regions (Gill, 1973; Matano et al., 2002).

Project administration:

E. P. Abrahamsen, M. P. Meredith,
A. C. Naveira Garabato, E. Frajka-Williams

Resources: E. P. Abrahamsen,
M. P. Meredith, A. C. Naveira Garabato,
E. Frajka-Williams

Supervision: E. P. Abrahamsen,
M. P. Meredith, A. C. Naveira Garabato,
C. P. Spingys, E. Frajka-Williams

Writing – original draft:

C. D. J. Auckland

Writing – review & editing:

C. D. J. Auckland, E. P. Abrahamsen,
M. P. Meredith, A. C. Naveira Garabato,
C. P. Spingys, E. Frajka-Williams,
A. L. Gordon

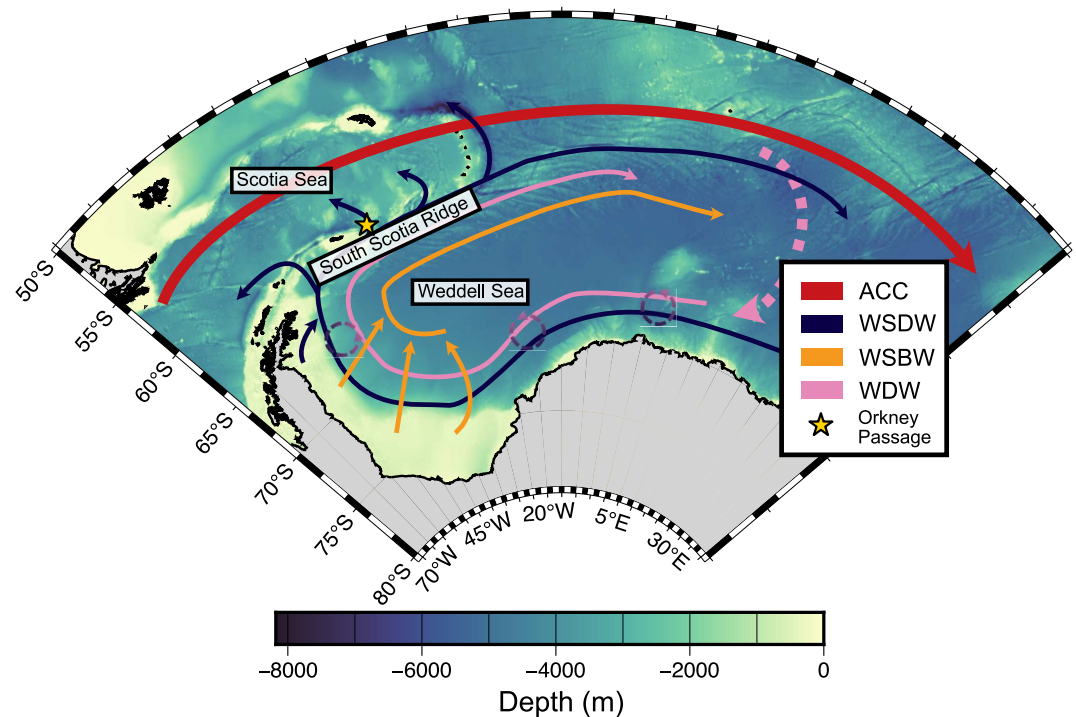


Figure 1. The bathymetry of the Weddell and Scotia Seas with the major water masses that contribute to Antarctic Bottom Water marked with their circulation. Warm Deep Water (WDW) entrained from the Antarctic Circumpolar Current (ACC) circulates within the gyre, mixing with cold, saline waters along the continental shelf and forming Weddell Sea Deep Water (WSDW) and Weddell Sea Bottom Water (WSBW). The lighter of the two, WSDW, may escape the gyre through a series of gaps in the South Scotia Ridge (SSR) system.

Weddell-sourced AABW is comprised of two water masses: Weddell Sea Bottom Water (WSBW) and Weddell Sea Deep Water (WSDW). WSBW is formed through a mixture of Warm Deep Water (WDW), entrained from the Antarctic Circumpolar Current (ACC), and cold, saline waters along the continental shelf as shown in Figure 1 (Fofonoff, 1957; Foster & Carmack, 1976; Gill, 1973). It is the densest Weddell Sea water mass, with a neutral density $\gamma^n > 28.40 \text{ kg m}^{-3}$. WSDW is lighter, $28.26 \text{ kg m}^{-3} < \gamma^n \leq 28.40 \text{ kg m}^{-3}$, and is formed through further mixing of WSBW and overlying WDW. Gordon et al. (1993) highlight that the mixing of shelf waters and WDW can directly produce WSDW. This fresher variety of WSDW is less dense, with a neutral density of $28.26 \text{ kg m}^{-3} < \gamma^n \leq 28.31 \text{ kg m}^{-3}$. The 28.31 kg m^{-3} isopycnal separates WSDW into upper WSDW (uWSDW) and lower WSDW (lWSDW), the latter of which is topographically trapped within the Scotia Sea (Naveira Garabato et al., 2002).

From their formation regions in the southern and western Weddell Sea, these dense waters flow northward in an abyssal boundary current along the eastern continental slope of the Antarctic Peninsula before encountering the South Scotia Ridge (SSR) system. The SSR acts a bathymetric barrier deflecting denser classes of WSDW and WSBW along the ridge eastward and retaining them within the Weddell Sea. The lighter classes of WSDW overflow the ridge through a series of deep passages, accounting for approximately half of AABW export from the Weddell Sea (Naveira Garabato et al., 2002). The most significant northward transport is through Orkney Passage (OP), the deepest passage that cuts through the ridge, with a depth of 3,650 m accounting for over 65% of dense water transport over the ridge (Naveira Garabato et al., 2002). As the boundary current flows through OP, the core of the current deepens and narrows across the sill into the Scotia Sea. Alongside this, the current becomes less dense as it transits OP due to intense mixing caused by instabilities generated by interactions between the flow and the steep, rough bottom bathymetry. This turbulent mixing is elevated by weak stratification in the bottom boundary layer, as a result of an enhanced downslope Ekman flow associated with the boundary current's flow along the sloping topography (Naveira Garabato et al., 2019; Polzin et al., 2014; Spingys et al., 2021).

Since 1990, AABW has experienced a marked contraction, warming, and freshening (Abrahamsen et al., 2019; Jullion et al., 2013; Purkey & Johnson, 2012, 2013; Strass et al., 2020). In addition, WSDW export shows significant seasonal and interannual variation (Gordon et al., 2010, 2020; Llanillo et al., 2023; Meijers et al., 2016; Meredith et al., 2008, 2011; Su et al., 2014). These shorter-timescale changes have been attributed to several mechanisms, many of which highlight the role of wind forcing in driving changes in export. As the Weddell Gyre is at least partly wind-driven, it can be expected that variations in wind could impact export (Armitage et al., 2018). The westerlies at the north of the gyre have experienced a multidecadal intensification and poleward shift associated with an intensified Southern Annular Mode (SAM). Alongside this multidecadal trend, various studies have highlighted wind forcing as a contributing factor to changes in export and formation across monthly, annual and interannual timescales (Gordon et al., 2020; Jullion et al., 2010; McKee et al., 2011; Meredith et al., 2008, 2011; Su et al., 2014; Wang et al., 2012; Zhou et al., 2023).

When seeking to diagnose the causes of changes in AABW export, it is important where possible to deconvolve changes in its production rate or properties from those in circulation rates or pathways. Abrahamsen et al. (2019) investigated variations in AABW volume in the Scotia Sea, and concluded that the decadal-scale downward trend in Scotia Sea dense water volume—and its recent hiatus—are due to changes in the rate of supply from the Weddell Sea. Over these decadal timescales, changes are attributed to variation in WSBW volume which modifies the depth at which the overlying WSDW layer sits within the water column. Variability in WSBW volume reflects changes in formation around the periphery of the Weddell Gyre caused by perturbations in sea ice production and freshening shelf waters. Anomalous wind forcing has been shown to impact the rate of sea ice formation, with reducing sea ice cover creating less saline shelf waters and decreasing WSBW production (Gordon et al., 2010; McKee et al., 2011). Strengthening westerlies additionally increase ice shelf melt and glacial discharge, which freshen the shelf water (Darelius et al., 2016; Jullion et al., 2013). Freshening can also be directly linked to wind forcing as changes in the strength of the boundary current move the shelf front, allowing greater injection of freshwater (Gordon et al., 2020).

Whilst these changes act on multi-annual timescales, observational studies of AABW volume show a rapid response in export to surface forcing on a timescale of a few months (Jullion et al., 2010; McKee et al., 2011; Meijers et al., 2016; Meredith et al., 2011). This rapid response suggests a barotropic adjustment in the circulation, due to the difference in propagation times of baroclinic and barotropic waves. Meredith et al. (2011) propose that a key mechanism involved is the response of the bottom Ekman layer to barotropic changes in the boundary current strength. The barotropic acceleration of the boundary current forces water toward and down the sloping topography. The increased down-slope current advects lighter water down the slope, bending and steepening the isopycnals in the passage (Brink & Lentz, 2010; MacCready & Rhines, 1993). The isopycnals continue to bend downward, creating a pressure gradient via which buoyancy forces arrest the down-slope motion. This produces a thick bottom boundary layer, reducing the transport through OP. The downslope flow weakens the stratification in the water column, creating conditions favorable for turbulent mixing processes that further lighten the dense water flow through OP (Naveira Garabato et al., 2019; Polzin et al., 2014; Spingys et al., 2021).

In addition to the barotropic mechanism described above, there will likely be a gyre-wide baroclinic response to changes in surface wind forcing (Coles et al., 1996; Meredith et al., 2008). Increased winds accelerate the gyre's cyclonicity, causing a steepening of isopycnals around the edge of the gyre and hence acting to deepen the upper boundary of IWSDW and progressively restrict the export of dense waters across the sill of OP. Given the characteristic timescale of a gyre response to changes in forcing, it is expected that this process will act across multi-year timescales (Jullion et al., 2010). However, Su et al. (2014) present an alternate baroclinic mechanism acting instead across monthly timescales. They propose that surface forcing excites small baroclinic oscillations in the gyre, which, due to mass conservation, lead to a thin boundary layer around the edge where oscillations counter those in the gyre's interior. This results in downwelling, through mesoscale eddies, at the gyre boundary, thereby restricting dense water export.

While several mechanisms controlling export variability have thus been postulated, their relative importance on different timescales remains unclear. Across timescales shorter than 18 months, we may expect transport variability to be largely controlled by changes in export pathways and gyre circulation, rather than changes in production rates or properties. In particular, the initial response is likely to be barotropic, though possibly modulated by local baroclinic effects in the bottom boundary layer. In this paper, we seek to test the applicability of these theory-based concepts to the ocean. We examine the drivers of interannual variability using mooring data from

within the boundary current that carries WSDW from the Weddell Sea through OP, in order to assess the extent to which export is controlled by wind and to determine the mechanisms linking such wind forcing to deep water export. In Section 2, we introduce the moorings, wind data, and statistical methods used in the study. In Section 3, we compare the observed temperature and salinity time series in each mooring. Following this, we present the observed changes in WSDW transport through OP in comparison with observed changes in the surface wind stress across the gyre. In Section 4, we discuss the likely mechanisms controlling the observed changes in transport, before presenting our conclusions and the implications of our findings in Section 5.

2. Data

Our investigation uses two sets of moorings within the Weddell Sea, as well as atmospheric reanalysis data, to examine the role of wind forcing in controlling WSDW transport through OP.

2.1. Orkney Passage Moorings

An array of five moorings was deployed in early 2011 across the saddle point of OP, covering the deepest part of the passage. A sixth mooring was added in the east of the passage in 2012, with the positions of the moorings shown in Figure 2. As detailed in Spingys et al. (2021), the mooring array consists of various combinations of current meters and temperature, temperature-pressure, and temperature-pressure-conductivity sensors. Temperature, conductivity, velocity and pressure are recorded approximately every 15 min before being averaged to daily means for our study. This range of instrumentation allows time-varying potential temperature, salinity and neutral density to be calculated across the array, and hence quantification of the variability in AABW transport and properties through the passage. Each moored instrument was calibrated before and after deployment from CTD casts taken during deployment and recovery.

Of particular importance to this study is the mooring OP2, which is situated at the steepest part of the slope on OP's western boundary. This mooring extends down to approximately 3,050 m and captures the core of the abyssal boundary current as it travels through the passage. As such, it provides a direct link between waters in the gyre's interior and those exported through OP. The bottom temperature-pressure-conductivity instrument lies 30 m above the seafloor with similar instrumentation approximately every 650 m vertically, with slight variation between redeployment years. Interspersed between these instruments are current meters, allowing the transport to be calculated.

OP2 has been deployed quasi-biennially since 2011, with the data used in our study from 2011 to 2019. Between April 2015 and April 2017 the mooring array was greatly enhanced as part of the Dynamics of the Orkney Passage Outflow (DynOPO) project (Naveira Garabato et al., 2019). This enhanced array greatly increased the vertical resolution with temperature sensors every 50 m and temperature-pressure-conductivity sensors approximately every 150 m. In order to remove the effect of high-frequency oscillations, the time-series were filtered with a fifth-order 60 day length Butterworth filter forwards and backwards in time.

As with OP2, the mooring array has been deployed biennially in the same configuration, seen in the inset of Figure 2 across the sill of the passage. The depths, and coordinate positions of each mooring are listed in Table 1 for the 2015–2017 deployment. For full details of the moored instrumentation and configuration please refer to the JR16005 cruise report (Naveira Garabato, 2017). The locations and depths for this deployment are representative of the time series as a whole.

In order to calculate water mass transport through the array daily values of current speed, temperature and salinity are bilinearly interpolated onto a regular grid covering OP of approximately 350 m horizontal and 9 m vertical resolution. Following the methods of Abrahamsen et al. (2019) and Spingys et al. (2021), a low-pass fifth-order Chebyshev Type I filter with a 400 m cut off wavelength is applied in the vertical dimension to temperature, pressure, salinity, and velocity, with any data interpolated farther than the distance between two adjacent moorings removed.

Transport is then calculated from the rotated velocities normal to the mooring array and the total cross-sectional area of each water mass. Neutral density is calculated as per Jackett and McDougall (1997). The array fully captures variability in IWSDW ($28.31 \text{ kg m}^{-3} \leq \gamma^n < 28.40 \text{ kg m}^{-3}$), but does not fully cover the lighter water masses as in some cases the lightest WSDW isopycnal is shallower than the top instrument of the array. As such,

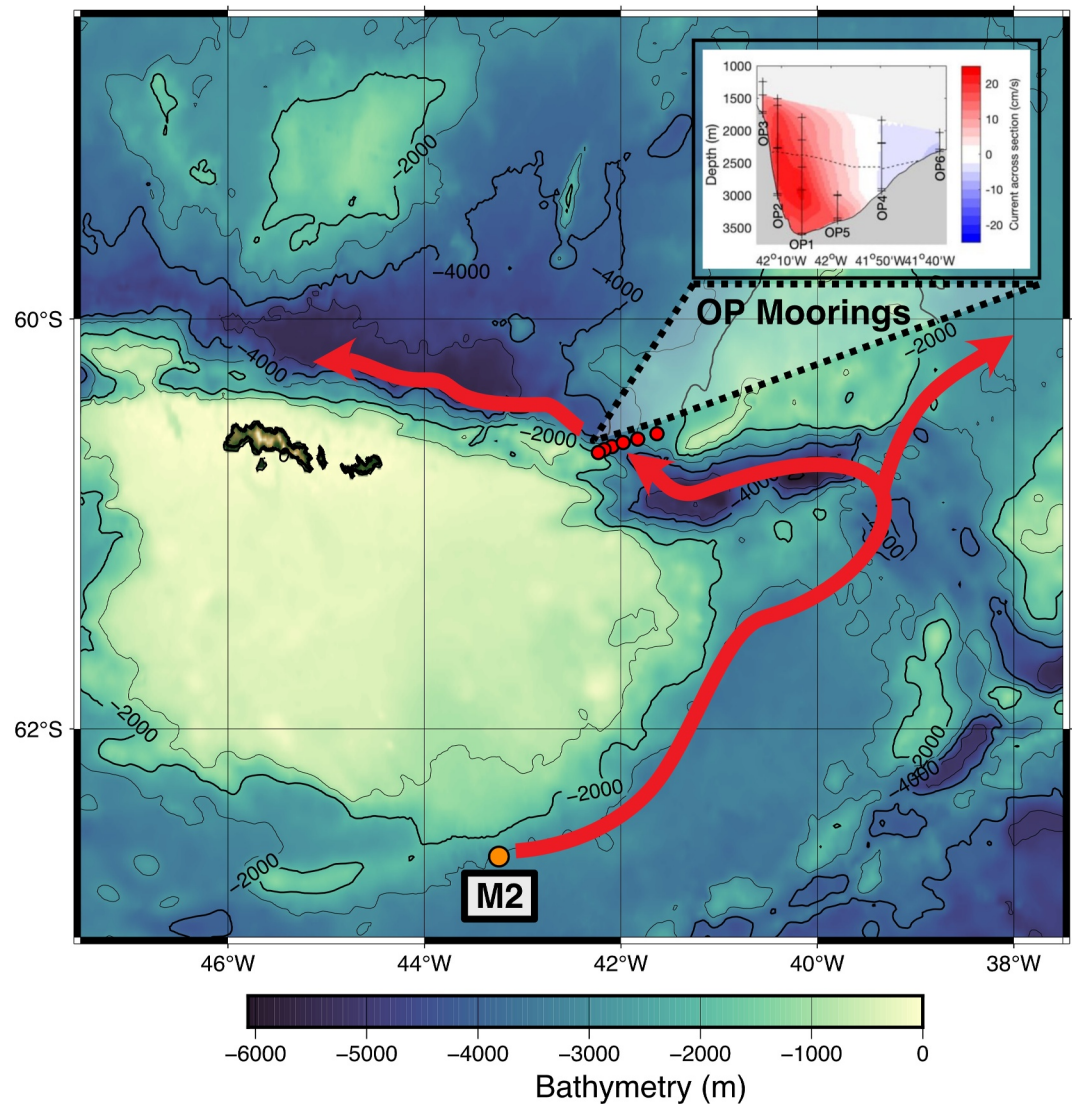


Figure 2. Bathymetry of the northwestern Weddell Sea with the locations of OP2 and M2 moorings highlighted. The OP mooring array is situated in OP with Orkney Plateau to the west. Red lines indicate the flow path between the moorings. Inset: OP mooring array configuration and location of each mooring in the passage. Each vertical line represents the position of a mooring in the passage, with the horizontal lines indicating the depth of each sensor on that mooring. The contoured background is the average velocity in the passage with the $\sigma_t = 28.31 \text{ kg m}^{-3}$ contour marked as a dashed line indicating the upper boundary of IWSDW. Velocity data is taken from instruments on the moorings and interpolated to cover the passage, more detail in Section 2.1. Figure adapted from Abrahamsen et al. (2019).

Table 1
Mooring Array Positions and Depths for 2015–2017 Deployment

Mooring	Deployment	Recovery	Latitude	Longitude	Depth
OP1	05/04/15	15/04/17	60°37.522'S	42°05.761'W	3,644 m
OP2	04/04/15	14/04/17	60°38.173'S	42°10.714'W	3,036 m
OP3	03/04/15	19/04/17	60°39.322'S	42°13.801'W	1,738 m
OP4	07/04/15	21/04/17	60°35.434'S	41°49.752'W	2,972 m
OP5	06/04/15	19/04/17	60°36.424'S	41°58.531'W	3,423 m
OP6	06/04/15	20/04/17	60°33.727'S	41°38.033'W	2,338 m

in areas where the dense waters overflow the array, we extrapolate upwards to the uWSDW upper isopycnal following the methods of Spingys et al. (2021).

2.2. LDEO Moorings

In order to investigate the influence of variability originating upstream of OP, data from the M2 mooring were examined. M2 forms part of the Lamont-Doherty Earth Observatory mooring cluster, which monitors properties of WSDW and WSBW in the Northwestern Weddell Sea (Gordon et al., 2010). The locations of M2 and OP2 are shown in Figure 2. M2 was selected as it is on the flow path of the lighter waters formed around Larsen Ice Shelf that are exported through OP. The mooring has a nominal depth of 3,050 m and

records temperature, pressure, conductivity and velocity. The bottom instrument analyzed has a depth of 3,000 m. The moorings have been deployed on an approximate 2 yr rotation; however, due to instrumentation failure or failed recovery, there is only partial temporal coverage between 2011 and 2019, the period covered by the OP array. The data from M2 underwent similar processing to that of OP2, using the same filter design.

2.3. Climate Data

Wind stress and wind stress curl were calculated from the ERA5 reanalysis product provided by the European Center for Medium-Range Weather Forecasting (Hersbach et al., 2020). ERA5 provides wind stress from zonal and meridional wind speeds by calculating the stress due to turbulent interactions between the atmosphere and surface as well as orographic form drag. It provides a regular 0.25° grid, from which stress curl can be calculated. The monthly averaged data time series was selected for analysis using the monthly northward and eastward stress outputs with a land mask applied. These values were used for calculation of wind stress curl with average values for specific regions calculated as the area weighted mean from the given latitude longitude grid points.

3. Results

3.1. OP2 Mooring

Figure 3 shows the potential temperature in the bottom instrument of the M2 (blue) and OP2 (orange) moorings with depths of 3,040 m and 2,990 m respectively. Initially, M2 and OP2 are relatively cool with temperatures of -0.50°C and -0.45°C before warming (by up to 0.025°C at OP2 and 0.05°C at M2) in late 2011 and early 2012. In early 2015, M2 and OP2 entered a warmer phase with temperatures up to -0.44°C at M2 and -0.42°C at OP2 before cooling in the second half of 2015 into 2016. This pattern of warming was repeated in late 2017 through 2018 with OP2 warming from -0.45°C to -0.43°C and M2 warming up to -0.47°C . There was no M2 deployment between 2014 and 2015, and a battery failure in the deep instrument on M2 in 2016; as such, there are no data for these periods.

These moorings are situated on the flowpath of IWSW transported northward through OP. As such, we expect that property changes found at the upstream M2 mooring are advected to OP2 by the abyssal boundary current. In order to examine changes to the boundary current, we perform a cross correlation analysis for temperature between the two moorings. A 60 day fifth order low-pass Butterworth filter was applied to both time-series to remove the influence of short lived spikes and even shorter term phenomena such as tidal signals. Following this, the long term linear trend was removed from each time-series. Due to the gaps in the data series we consider 1 yr segments where there were no gaps present. The cross correlation function was then calculated for each segment with a maximum lag period of 180 days. To estimate the significance of these correlations we calculated the auto-correlation integral timescale adjusting the effective degrees of freedom for each time series accordingly (Thomson & Emery, 2014). The estimated lag period in the signal is reported as the interval where the cross correlation function of the temperature signals was greater than the 95% significance threshold calculated from the effective degrees of freedom.

Temperatures at M2 and OP2 are positively correlated for large sections of the series, with the strongest correlation in 2015 through 2016 ($r = 0.7$ significant at the 95% level with six effective degrees of freedom). Calculating the cross correlation between the time series during the warm anomaly in 2015 showed a lag of 32 ± 8 days, with anomalies in M2 leading those in OP2, as expected due to M2's upstream positioning in the boundary current. Outside of these warming anomalies the characteristic lag time was an order of magnitude greater, varying between 100 and 200 days. The shortest lag time corresponds to a flow speed of 12.5 cm s^{-1} , concomitant with the warm anomalies based on an assumed distance along the advective path between the moorings of 350 km. The transition between the long and short-lag regimes is difficult to assess for the 2015 anomaly without the preceding temperature data from M2, but cannot exceed a period of more than a year. For the transition in 2017 through 2018, this transition is rapid with a timescale of just a few months.

Figure 3 shows the practical salinity in M2. Between 2011 and 2014, M2 shows a slight freshening trend concentrated around mid 2012. This was followed by a period of substantial freshening between 2015 and 2016. This freshening maximum occurs somewhere in mid 2016, but due to the instrumentation failure its exact timing is not clear. This freshening lags the raised temperature anomaly by approximately a year. This could indicate that

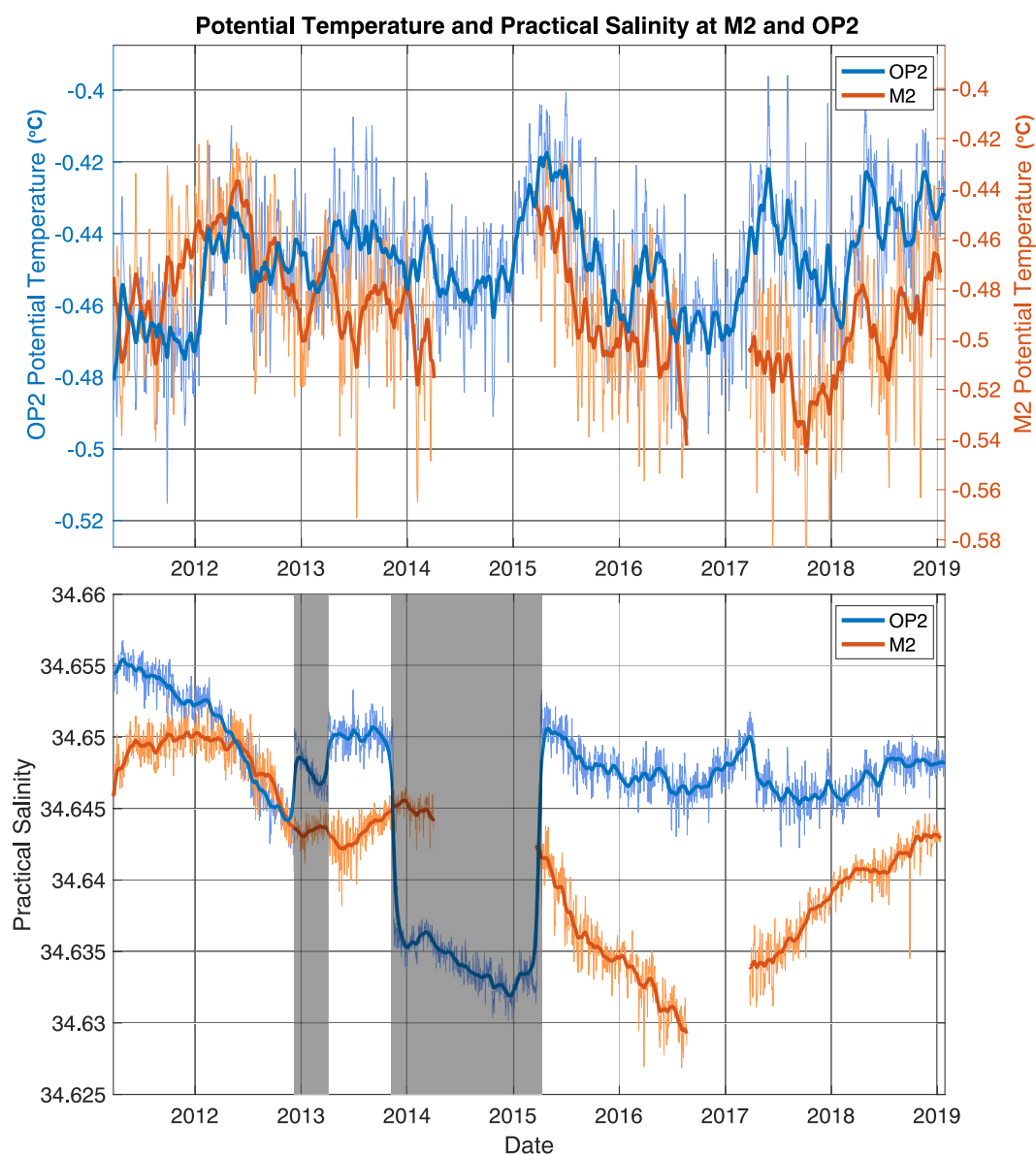


Figure 3. Upper Panel: Potential temperature in the bottom instruments of OP2 (blue) and M2 (orange). A 60 day Butterworth low-pass filter has been applied to the data (thick) with the daily average behind (thin). Please note the different scales for each instrument. Lower Panel: Practical salinity measured in the bottom instruments of the M2 and OP2 moorings. Practical salinity was calculated from direct observation of conductivity, temperature and pressure. The gaps in the time series correspond to periods in which the instruments were not deployed or battery failure in 2016–2017 for M2. The gray-highlighted area shows periods of offset in OP2 measurements. The instruments were calibrated before and after deployment against CTD casts, however no offset was found.

mechanisms controlling salinity have different timescales to those controlling temperature, discussed later. From 2017, the salinity began to recover to its previous levels.

The salinity time series for OP2 in Figure 3 is more challenging to interpret, as there is a clear disjoint in salinity in late 2013, likely instrumental in origin. The freshening in 2012 in the M2 sensor also appears in OP2; however, due to the quality of data, a lag period cannot be readily determined. We instead focus on the 2015–2019 period, where we again find strong freshening in late 2016. In the 2017–2019 redeployment, salinity slightly recovers. Due to the inconsistent nature of OP2, cross correlation analysis of the salinity measurements is not feasible; however, the broad trends apparent at M2 appear in the individual OP2 mooring time series.

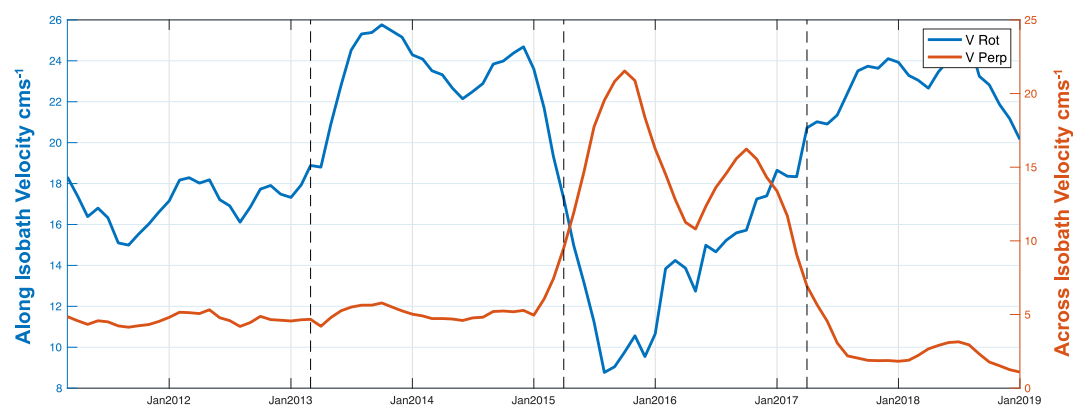


Figure 4. Velocity in the bottom instrument of OP2 rotated to be oriented in the direction of the passage $\approx 344^\circ$ to geographic north. The velocity was decomposed into the along slope (blue) and across slope (orange) components. Dashed lines indicate time periods of mooring redeployment as within the bottom boundary layer velocities can be sensitive to depth changes.

Figure 4 shows the velocity rotated and decomposed into the along slope and across slope components. The measurements are taken from the bottom velocity instrument on the OP2 mooring with an approximate depth of 3,000 m. This instrument is within the boundary layer for the flow through OP throughout the measurement period and shows a considerable across slope increase in velocity concomitant with the period of warming observed in 2015. Similarly the along slope velocity approximately halves from a mean of 21 cms^{-1} outside of this time to a minimum of 9 cms^{-1} in late 2015 before recovering.

3.1.1. Enhanced OP2 Mooring Between 2015 and 2017

As detailed in Section 2.1, additional instrumentation was added to the OP2 mooring between April 2015 and 2017. The greater resolution allows for a more detailed look at changes to the core of the abyssal boundary current. The enhanced instrumentation was fortuitously concomitant with the warming and a boundary current intensification in 2015–2016. An increase in cross-slope near-bottom velocity can be seen from direct measurements in Figure 5. The positive (downslope) anomaly is concentrated in the bottom 200 m of the moored instrument. The downslope velocity anomaly is concomitant with a bottom-intensified warming through this period, extending 1,200 m from the bottom. This is accompanied by a reduction in neutral density across the water column, again bottom-intensified. Such reduced density contributes to the reduced IWSDW transport evident in panel (d).

By January 2016, both the warming and downslope velocity anomaly have greatly decreased in intensity and begun to reverse. At this time, the transport anomaly begins to increase, and this increase continues for the rest of the period. The neutral density anomaly does not fully reverse until 7 months later. However, the lowest 500 m, in which the majority of the IWSDW resides, begins to increase in density earlier than the rest of the water column. A further explanation for this is that the anomalies are referenced against the period in the figure, when we already have reduced transport through the passage. Therefore, while the anomaly may appear positive, it may still be negative in comparison to the longer-term mean.

3.1.2. Wavelet Transforms

To further investigate the variability in the lagged cross correlation, a wavelet transform was applied to each time series, and the wavelet transform coherence was calculated. The wavelet transform expands the time series in time-frequency space, highlighting the temporal variability in the power spectrum. This analysis used the MATLAB wavelet toolbox developed as part of Grinsted et al. (2004). The continuous wavelet transforms use the Morlet wavelet with a center frequency of $\omega_0 = 6$. As the Morlet wavelet is complex, this returns information about the phase, allowing a comparison of the lag periods calculated in the cross wavelet transform. Significance was calculated using a Monte Carlo simulation ($n = 1,000$) with a null AR-1 red noise spectrum for both the wavelet transforms and coherence.

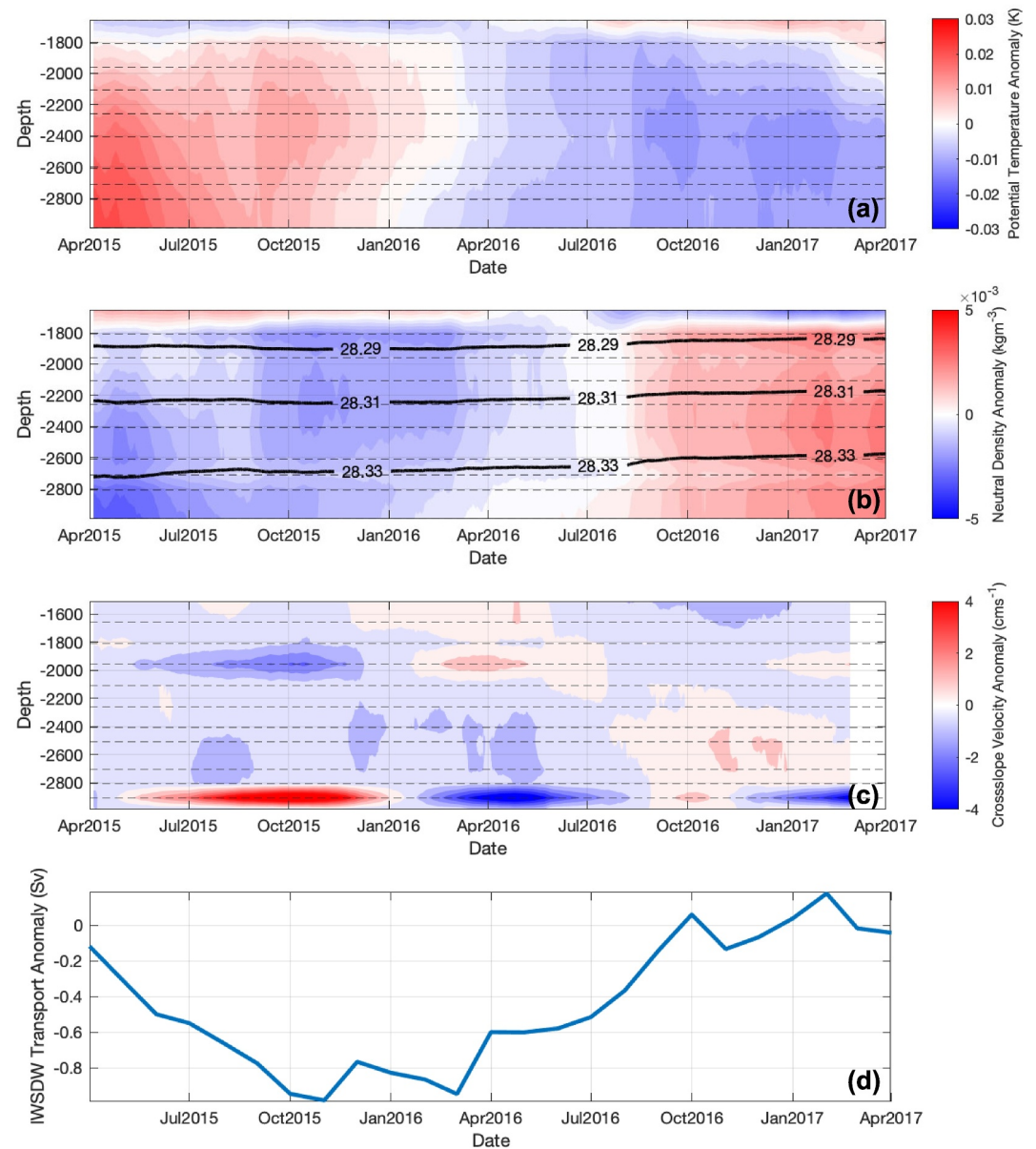


Figure 5. Panels constructed from April 2015 to April 2017, the period in which there was an enhanced mooring array as part of the Dynamics of the Orkney Passage Outflow (DynOPO) project. Displayed are (a) Potential temperature anomaly, (b) neutral density anomaly, contours of neutral density are marked to show the contraction and thickening of layers, (c) cross-slope velocity anomaly, and (d) IWSDW transport through OP. For panels (a)–(c), the anomaly was calculated for all instruments along the OP2 mooring. The anomaly was taken with respect to the depth mean for each instrument. A 12 month moving mean was then applied to the data to make it comparable with previous analyses. The dashed lines indicate the instrument nominal depths.

Due to the instrumentation failure in the bottom instrument of the M2 mooring, the gaps in the time series were filled by binning the M2 data into daily averages and applying a second-order spline function to interpolate the missing data periods. This produced a signal similar to that seen on the annual timescale for the OP2 data however removes significant power from the sub-annual signal for this instrument (seen by the conical shadow in Figure 6).

Both moorings display significant power at periods longer than 256 days, with a peak in the power spectrum at periods of 3 yrs as seen in Figure 6. These time frames show that there is significant annual and interannual variation in the moorings, the longest time frame corresponding to the length of time between consecutive warming anomalies in each mooring.

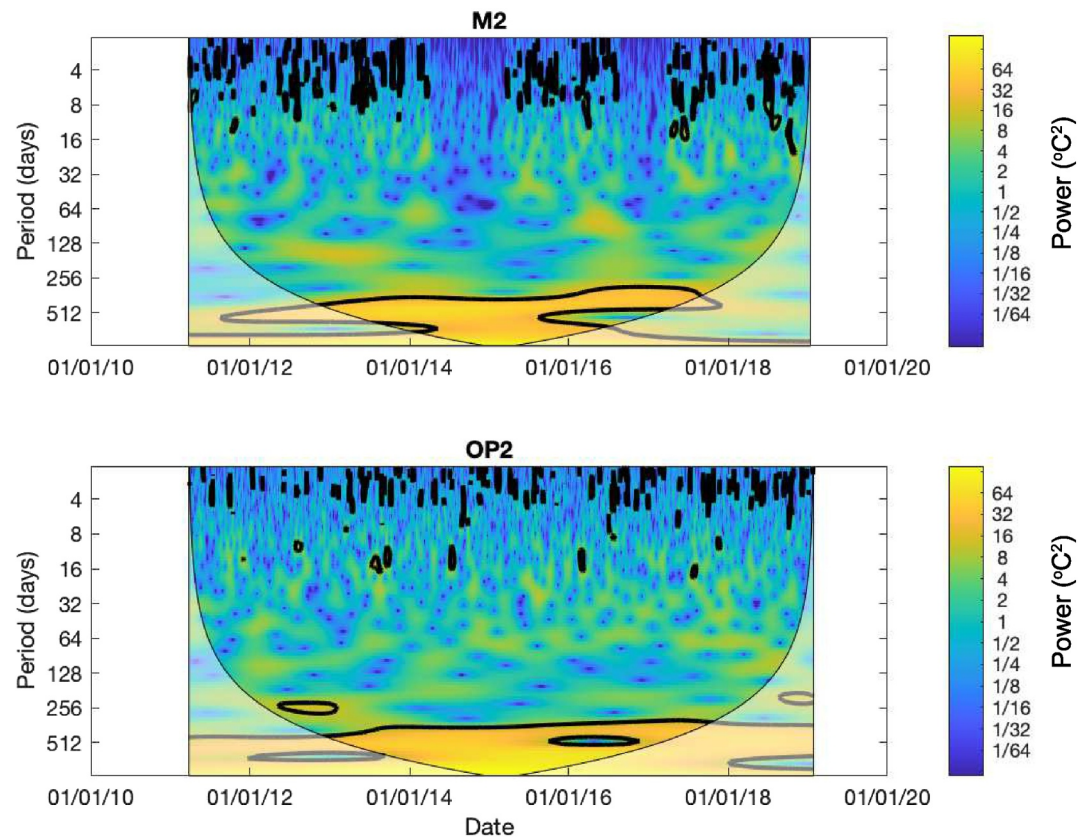


Figure 6. Wavelet transforms of the potential temperature measured at OP2 and M2. The transforms show the variation in power of the mooring spectrum against time on the *x*-axis and period on the *y*-axis. The black contours show areas of 95% significance. The shaded section indicates the edge of the cone of influence.

Calculating the wavelet transform coherence confirms the shared power at these frequencies (Figure 7). We can estimate the lag times between the two series for this period using the phase angle and wavelength. Calculating the circular mean of the angles within the 95% significance region around this 1 yr period, and then converting to a lag period, shows that M2 leads OP2 by 81 ± 23 days in late 2013 and early 2014. The estimates of phase difference are consistent with the time periods found from the lagged cross correlation. Similarly mid 2014 values of 75 ± 15 days are consistent with lagged cross correlation calculations although the signal from M2 is interpolated for this period significantly reducing confidence in the phase difference calculation.

The lead time reduces to 28 ± 12 days during 2015 as the phase angle lessens, which is broadly consistent with values calculated using cross correlation. The cross wavelet transform phase angle is calculated only for the significant period in the 1 yr band, which acts in a similar fashion to a band-pass filter. This removes variability in the signal at wavelengths longer and shorter than this period, which may have different lead/lag relationships.

3.2. Orkney Passage Transport

Figure 8 shows the northward transport of IWSDW through OP between 2011 and 2019. Northward transport displays considerable high-frequency fluctuations throughout the time period, and in some extreme cases transport is actually reversed through the passage in 2012, 2015 and 2016. These reversals are short-lived, and are a consequence of anomalously strong return flow on the eastern flank of the passage or a complete cessation in transport in the west. To focus on the annual and interannual variability, we applied a 12 month running mean to the time series. Between 2012 and 2014, the transport through the passage slightly increases before starting to decrease in the middle of 2014. By the middle 2015 the average transport was anomalously low, reducing by 1 Sv at the start of 2016. The start of the reduced transport period aligns with the warming anomaly in 2015, as well as a similar timescale for the freshening observed in 2016. The offset between the temperature and salinity

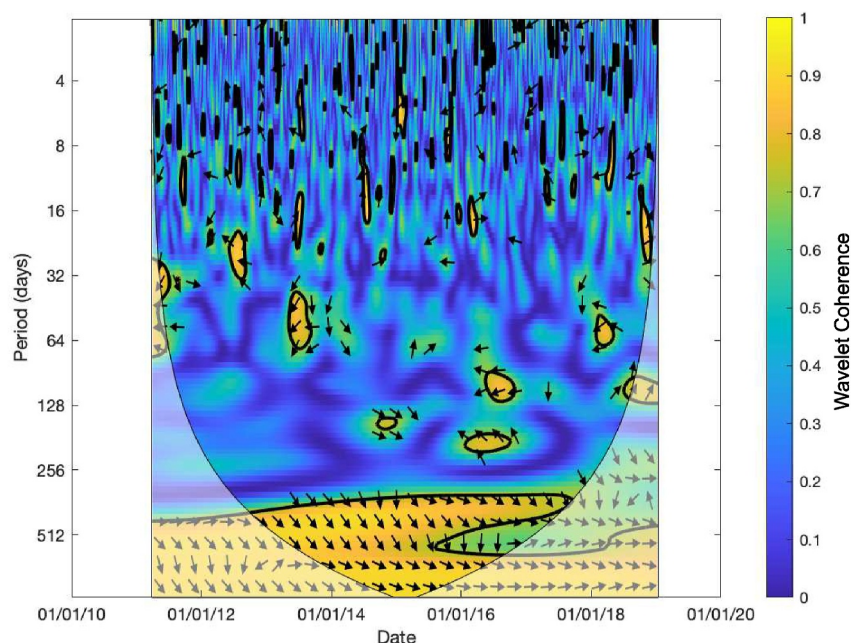


Figure 7. Wavelet Transform Coherence of the potential temperature measured in the bottom instrument OP2 and M2. Coherence is measured between the two transforms and highlights areas of similar power. The arrows shown are phase vectors, indicating the phase difference between the two time series with downward arrows indicating M2 leads OP2. The black contours show areas of 95% significance levels calculated via a Monte Carlo method.

anomalies may explain why the transport anomaly period was longer than observed in each individual variable, as both influence the water's neutral density.

Following this, there was a partial recovery in transport before slightly reducing again to the end of 2017. Transport through the passage partially recovered toward the 2014 values by the end of the time series although is still lower. Figure 8 also shows the changes in total WSDW transport through OP. This largely reflects the tendencies seen in IWSDW, as expected; however, we focus here on IWSDW, as the water passing through the bottom sensor of OP2 and M2 is composed of this denser class. Furthermore, due to the mooring array used in OP, the top section of WSDW is not fully captured, and has been inferred from interpolation of values upward from the nearest instrument based on CTD sections taken at the times of deployment.

3.3. Relationship Between OP Transport and Properties to Wind Forcing

To investigate the role of wind forcing on export variability, wind stress curl was calculated from the zonal and meridional gradients of the northward and eastward wind stress respectively between 62 and 70°S and 60–0°W with the area-integrated mean displayed in Figure 9 panel (a), alongside IWSDW transport through OP. This region was selected to capture the dynamics of the Weddell Gyre with boundaries chosen to match the previous study presented in Abrahamsen et al. (2019) Figure S4. Other boundaries were considered; including the gyre regions from Meredith et al. (2011) and Gordon et al. (2020); these are not shown here, but do not give significantly different results to those presented. Time series of zonal and meridional wind stresses are shown in panels (b) and (c) of Figure 9.

Wind stress curl across the gyre is anticyclonic between 2011 and 2019 and displays significant interannual variability with periods of intensification and weakening. In 2014 there is a short period of weakened curl across the gyre, before a prolonged period of intensification peaking in 2015 and de-intensification in the latter half of 2016. This is short-lived, with a shorter strengthened period in the summer of 2017, peaking in early 2018 before returning to average values. Further investigations of the variability of the zonal component of wind stress using Empirical Orthogonal Function (EOF) analysis, supplementary Figure S1 in Supporting Information S1, shows strong westerly winds centered around the SSR and the northern Weddell Sea, with easterlies along the southern

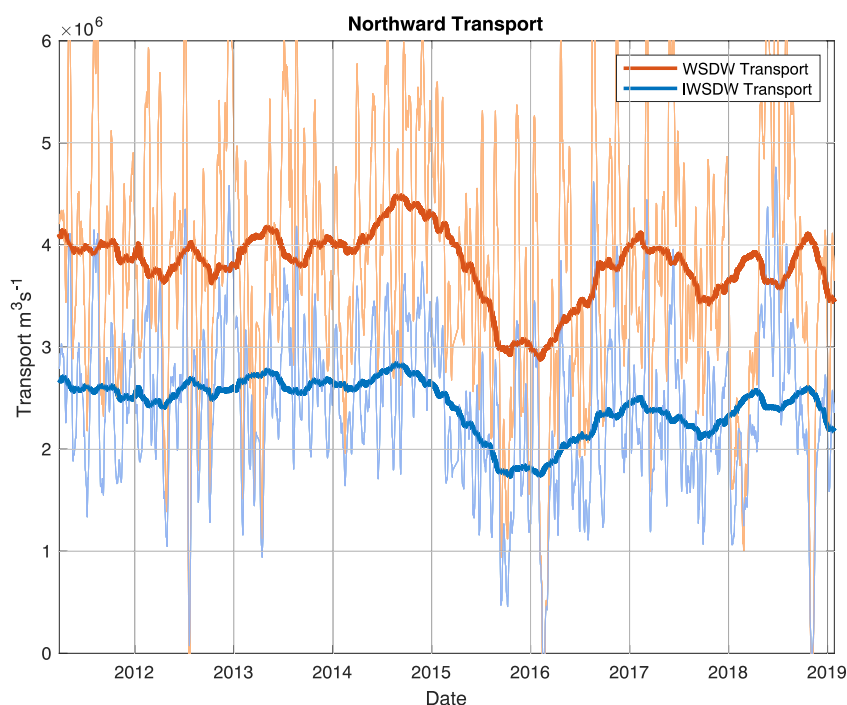


Figure 8. Northward transport of WSDW (orange) and IWSDW (blue) through OP as calculated using the interpolated grid from the mooring array, with a 12 month moving average (thick line). The area of each water mass was calculated and multiplied by the velocity measured. IWSDW mirrors the changes in WSDW total, as expected.

section. This large meridional gradient in zonal velocity dominates the wind stress curl calculation, and as such the principal component time series resembles that of the wind stress curl from Figure 9.

To capture local changes across the region of the moorings along the slope of the SSR, wind stress curl, zonal wind stress, and meridional wind stress were examined in the region between 60 and 63°S and 50°W–40°W as seen in Figure 9. A larger region across the entirety of SSR was considered too; however, due to the abyssal flow path of bottom water out of OP, the impact of wind stress east of Orkney Deep will not affect the northward abyssal transport and as such is not presented.

Using the smaller region focused on the SSR and the mooring locations we again see an intensification of wind stress curl in 2015, however, the gyre wide intensification in 2017 is not significant and is less pronounced across this smaller region. The signal in wind stress curl is again most consistent with the zonal wind stress for the region, as expected from the EOF analysis.

Surface wind forcing is hypothesized to impact both the density and volume of northward transport of AABW through OP as detailed in Section 1. Here we quantify how the observed properties through the OP mooring array correlate with the changes in surface forcing. Northward IWSDW transport through OP was averaged into monthly bins before a 12 months moving average was applied to the data to investigate interannual changes in transport. Subsequently the cross correlation between similarly treated ERA5 mean monthly fields was calculated with a maximum lag period of 12 months. The significance of this correlation was again estimated using the auto correlation functions to find the number of Effective Degrees Of Freedom (EDOF).

Initially the relationship between gyre wide wind stress curl was considered using the region described above. There is a moderate positive correlation ($r = 0.5$, significant at the 95% level, EDOF = 14) between curl across the gyre and transport with a lag time of 1–4 months estimated from the cross correlation function. This correlation is particularly strong for the 2015–2016 period, however subsequent periods of strong forcing in 2017–2018 are not reflected in observed transport variability suggesting gyre wide wind forcing is not a primary control on transport variability. Following this, we consider a smaller area in the region of the moorings and boundary current. Again we find a positive correlation ($r = 0.7$) with significant covariance occurring at lags of 0–3 months. Notably this

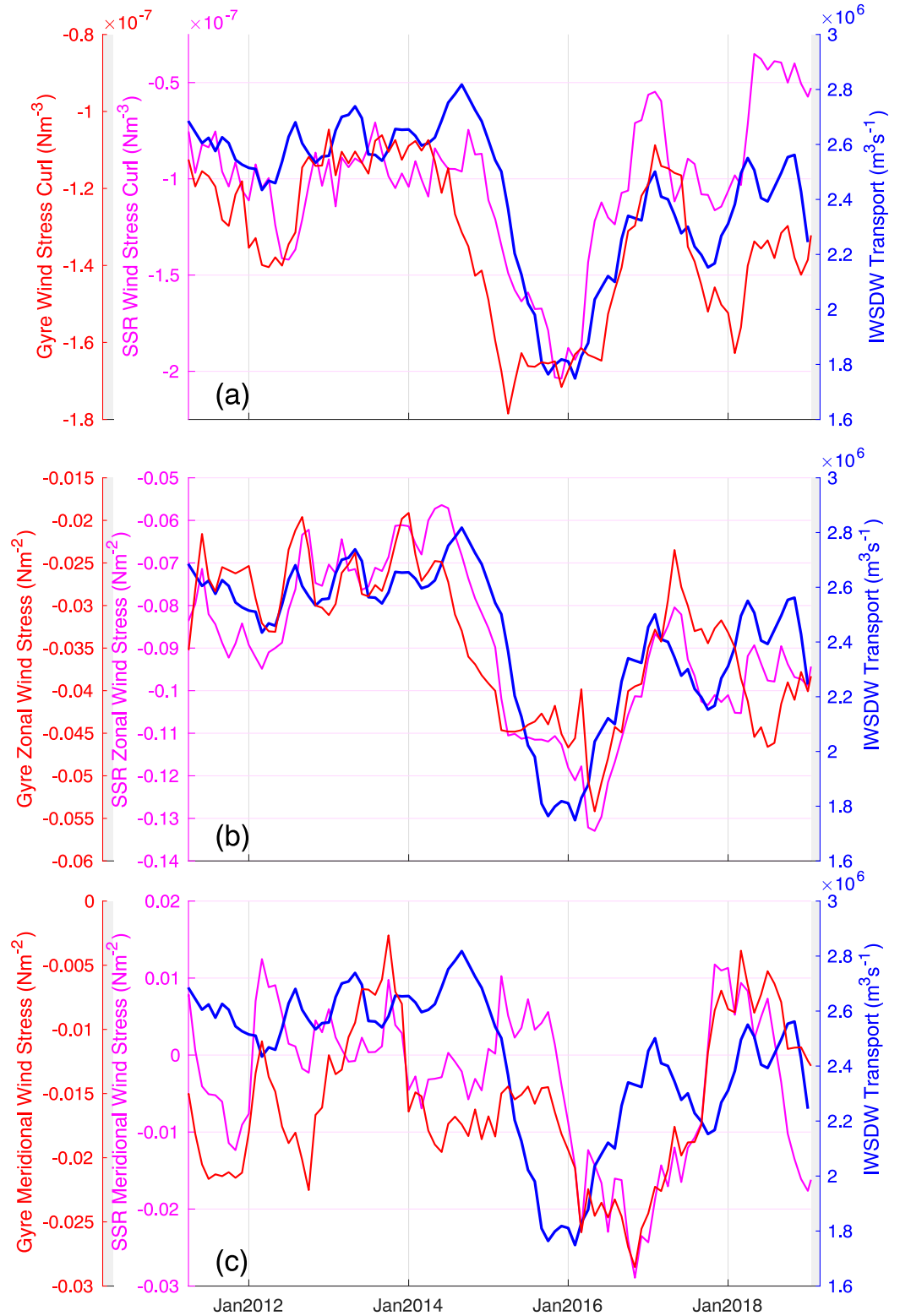


Figure 9. (a) Mean wind stress curl, (b) mean zonal wind stress, and (c) mean meridional wind stress. The mean values are calculated as the area weighted mean across the Weddell Gyre region 60°S – 70°S and 60°W – 0°W (red) and across the SSR region 60°S – 63°S and 50°W – 40°W (magenta). Note the flipped y axis on panels (b) and (c) for the wind stress. The total IWS DW transport is also plotted against each variable through OP (blue) from 2011 to 2019. A 12 months moving average was applied to all data.

local region shows reductions in wind stress curl and zonal wind stress in 2017–2018 compared to the gyre wide calculation and as a result is more highly correlated with observed OP transport.

To further examine regional significance, point wise correlations were calculated between the wind stress curl and the northward IWSDW transport through OP as shown in Figure 10. Significant strong positive correlations ($r \geq 0.75$) are found between the wind stress curl and northward IWSDW transport through OP in the region of the boundary current carrying IWSDW toward OP. This coherent relationship between local wind stress curl and transport is indicative of a dynamical link between wind forcing in the region and transport through OP. Similarly, Figure 10 shows the point wise correlation between northward IWSDW transport through OP and zonal wind stress with strong correlations found across the northern boundary of the gyre along the slope. Meridional wind stress was also considered, but not found to be significantly correlated. This is expected as wind stress is predominately zonal across the northern Weddell Sea and accounts for the majority of wind stress curl variance in this region. Examining the different lag periods shows a peak correlation between IWSDW transport and wind forcing with a lag of 0–2 months across SSR and Orkney Plateau. This relatively short timescale is similar to the timescale for the intensification of the boundary current found from the temperature time series and is consistent with previous studies work on wind forcing in the region by Meredith et al. (2011), Meijers et al. (2016), and Su et al. (2014). The rapid response to forcing and concurrent boundary current intensification suggests that changes to the barotropic boundary current strength link variability in surface forcing to transport as hypothesized by Meredith et al. (2011).

4. Discussion

The variable lead/lag relationship between OP2 and M2 indicates changes in velocity of the boundary current between the two moorings, as detailed in Section 3.1. Through 2015 and 2016, the reduction in transport of IWSDW through OP was coincident with increases in the boundary current velocity through OP, increased temperatures, and increasingly negative wind stress curl over the gyre. From Section 3.3 we find strong correlation between wind stress curl and zonal wind stress along the SSR with northward IWSDW transport through OP, suggesting the potential for a mechanism causing these variables to co-vary.

The response time of transport to intensified surface forcing is relatively rapid (no more than 3 months) and matches similar timescales found in previous studies (Jullion et al., 2010; Meijers et al., 2016; Meredith et al., 2011). These short time frames are indicative of barotropic changes in the flow through OP. The rapid transition between periods of long and short lag times found in the temperature time series also mirrors this time frame, adding further evidence that the mechanism linking the surface and bottom boundary current involves barotropic dynamics. As such, we propose that the initial reduction in transport is due to a barotropic acceleration of the boundary current induced by the increased zonal wind stress across the SSR and to a lesser extent wind stress curl in the region.

Armitage et al. (2018) showed how the Weddell Gyre responds to wind stress curl, with a near-instantaneous response in gyre intensity to changes in surface forcing being communicated gyre-wide by the propagation of barotropic waves. The initial period of forcing modifies the geostrophic transport across the gyre, with long periods of negative wind stress causing Ekman divergence and pushing water toward the gyre boundary. However, the Ekman suction and subsequent downwelling at the gyre's boundary is not sufficient to account for the observed changes in IWSDW transport. For typical rates of Ekman pumping, it would take in excess of 3 yrs to displace the isopycnals sufficiently to explain the observed transport changes. Instead, of greater importance is the barotropic acceleration of the boundary current. This acceleration is seen in the reduced lag times between the M2 and OP2 moorings during 2015 and 2016. As seen in Figures 9 and 10, transport responds to invigorated westerlies along the northern flank of the basin above the region of the IWSDW abyssal boundary current. These periods of surface forcing are concurrent with the decreased lag time in temperature anomalies between the moorings on the current path indicating that winds are responsible for the invigoration of the boundary current. This increase in boundary current speed causes subsequent changes to the northward transport within the passage, as detailed below.

4.1. Boundary Current Dynamics and Transport

The acceleration of the boundary current along the SSR will have a number of implications for transport through OP. Along sloping rough topography, such as the SSR, the invigorated boundary current will experience

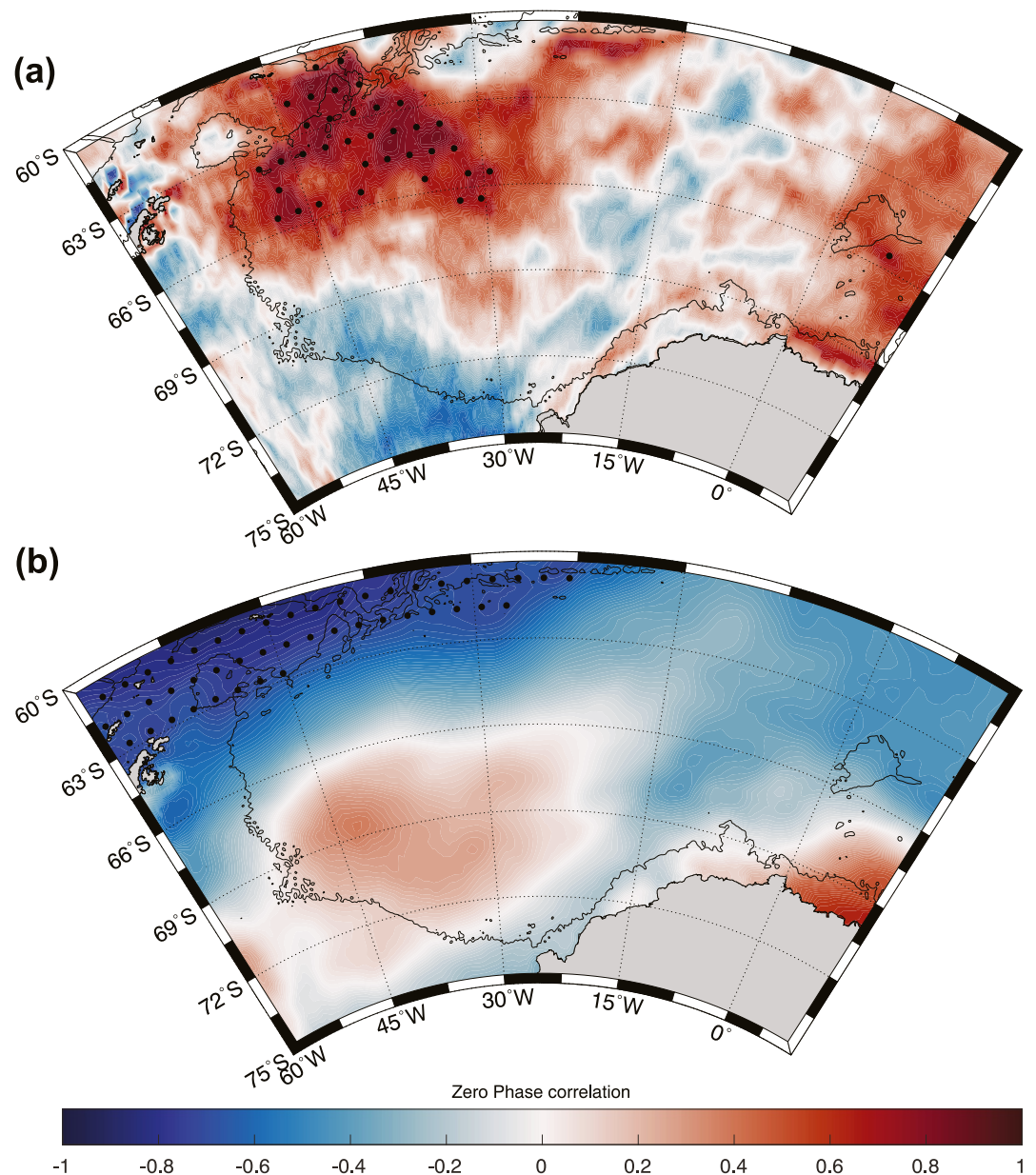


Figure 10. (a) Point-wise correlation of monthly ERA5 wind stress curl and IWSDW transport through OP with a 12 months moving average applied. (b) As in (a) but using ERA5 monthly zonal wind stress. Positive anomalies in zonal wind stress are Eastward with a negative correlation between transport and zonal wind indicating strong eastward wind is coincident with a reduction in transport. The black line indicates the 3,000 m contour highlighting the anticipated flow path of the bathymetrically controlled boundary current. The zero lag correlation is shown in the figure with stippling indicating the regions where correlation is significant at the 95% level.

increased bottom drag along the flowpath. In turn this drag will drive an increased downslope flow, with a compensating flow toward the boundary in the interior (Brink & Lentz, 2010; Garrett et al., 1993). This advects the lighter water masses to greater depth, destabilizing the water column and steepening isopycnals at the topographic slope interface (Brink & Lentz, 2010). The down-slope flow creates a pressure gradient, increasing the buoyancy forcing to counteract the downslope flow, before the flow's arrest when these forces are in balance. This mechanism causes a thick bottom boundary layer to develop with the steepened isopycnals, progressively restricting the volume of northward transport of the densest classes of WSDW.

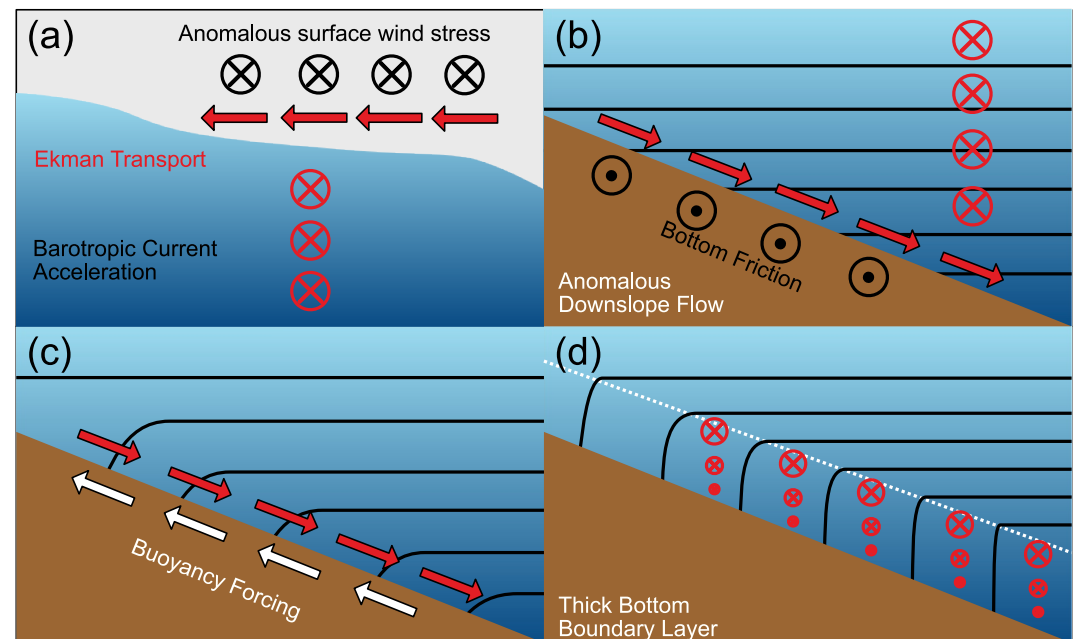


Figure 11. Schematic showing the changes in the bottom boundary layer. (a) Strong westerly wind stress at the surface drives anomalous barotropic acceleration in the water column. (b) The acceleration increases the bottom frictional force, causing an anomalous downslope flow and (c) bending the isopycnals as shown by the black lines. Counteracting this is buoyancy forcing acting against the down slope bringing the Ekman layer to arrest. The final panel (d) shows the thick bottom boundary layer, bounded by a dashed line, where the velocity decays to zero toward the slope.

Figure 11 shows an idealized schematic of the described mechanism. The mechanism causes a very thick bottom boundary layer to form (Brink & Lentz, 2010; Garrett et al., 1993; Polzin et al., 2014). The core of the abyssal boundary current through OP is mainly concentrated along the western flank; as such, anticipated changes in the bottom layer are also concentrated here. Inside this bottom boundary layer the velocity decays toward zero at the slope, which further reduces any transport of dense water masses in the layer. If the mechanism described is responsible for the reductions of transport within the passage we would expect to observe; (a) an increased boundary current velocity during periods of reduced transport, (b) rapid changes in boundary layer properties and transport as a consequence of this intensified boundary current, (c) increased downslope flow along the SSR and within OP, (d) bottom intensified anomalies in density and/or temperature; and (e) a reduction in northward transport within this bottom layer.

Regarding condition (a) of increased boundary current velocity, we have shown from our lagged analysis of temperature anomalies in Section 3.1 that temperature experiences a variable lead/lag relationship between the M2 and OP2 moorings. The boundary current along this region is topographically controlled, as such, changes to this time period represent changes in the currents velocity. During 2015–2016 the lag period was greatly reduced indicating an intensification of the boundary current. Observations of condition (b) are harder to determine using the moored cross correlation analysis. However, as detailed above, changes to the transport around the margins of the Weddell Gyre are connected to wind stresses and wind stress curl with strong periods of surface forcing accelerating the barotropic boundary current. As shown in Figure 9 we find a rapid response in transport to wind, and therefore boundary current intensification.

Regarding conditions (c) and (d), the observations from the enhanced OP2 mooring in Section 3.1.1, coincident with the boundary current acceleration and consequent transport reduction, show increased cross-slope near-bottom velocity. This is confined to the bottom 200 m of the mooring array, however the exact extent of the positive anomaly is hard to quantify as, even with the enhanced mooring, velocity measurements are only captured every 100 m. The increase in downslope flow causes advection of lighter masses to greater depths bending the isopycnals and creating a bottom intensified anomaly in both density and temperature as seen in Figure 5. This enhances the cross slope overturning circulation as, due to conservation of mass, we see a return flow toward the slope shown by the negative cross-slope velocity at approximately 1,900 m depth. This

overturning circulation mirrors that observed by Naveira Garabato et al. (2019) with the anomalies representing a strengthening of the overturning.

We observe condition (e) in the resulting transport time series. The increase in boundary layer thickness leads to a reduction in northward transport as along slope velocity decreases, with a contraction in the dense water layer thickness. This contraction is evident in Figure 5 displaying the IWSW contour, as transport recovers we see an uplift in the contour of approximately 90 m. Whilst this uplift is smaller than expected from the changes in boundary layer thickness predicted, it is important to note that this isopycnal has an approximate depth of 2,200 m which is an upper limit of the predicted layer thickness. Of greater significance is the reduction in along isobath velocity found within the boundary layer and shown for the bottom instrument of OP2 in Figure 4. This displays considerable similarity to the variance in transport with marked reduction in along slope velocities during the negative transport anomaly.

4.1.1. Layer Thickness

The thickness of the bottom boundary layer can be calculated from the Ekman dynamical framework laid out by Brink and Lentz (2010). From Equation 22 of Brink and Lentz (2010), the thickness of the downwelling-favorable boundary layer (h^D) is a function of the interior velocity (v_I), buoyancy frequency (N), Burger number (s), and Richardson number (Ri^D):

$$h^D = \left(\frac{v_I}{2Ns} \right) \left(1 + (1 + 4Ri^D s^2)^{\frac{1}{2}} \right). \quad (1)$$

This layer thickness is a measure of where the gradient of density profiles weakens from the linear gradient observed in the interior. We calculate an approximate layer thickness along the flow path between the M2 and OP2 moorings using the estimated abyssal boundary current intensity and typical values along SSR of $N^2 = 10^{-6} \text{ s}^{-2}$, $s = N^2 f^{-2} \sin^2 \theta = 0.12$ ($\theta \approx 2^\circ$), and $Ri = 0.1$. Initially the boundary current speed is reduced with $v_I \approx 4 \text{ cm s}^{-1}$, resulting in a boundary layer thickness of $h^D \approx 330 \text{ m}$. As detailed in Section 3.1, during 2015 we find a greatly shortened lag time corresponding to $v_I = 12.5 \text{ cm s}^{-1}$, which increases the thickness of the bottom boundary layer to $h^D \approx 1,000 \text{ m}$. This layer thickness assumes a uniform change in the interior velocity and constant buoyancy frequency. For the flow path along the SSR these are reasonable approximations however at the sill of OP the one dimensional Brink and Lentz model begins to break down due to the turbulent dynamics at the sill of the passage causing both buoyancy frequency, interior velocity, as well as Richardson number, to vary much more than along the SSR.

In reality, the expected change in boundary layer thickness is unlikely to be realized to the same extent as laid out by the theoretical framework. The changes in boundary layer thickness predicted by Brink and Lentz (2010) assume a step change in velocity, with steady flow and a uniform boundary slope. OP has several rough bathymetric features, making direct comparison challenging. The increased surface roughness in OP will cause increased bottom drag, and consequently an already thickened boundary layer against the Brink and Lentz (2010) estimates. Other mechanisms including baroclinic adjustment of the gyre structure, as suggested by Su et al. (2014) also act upon the boundary current system with similar timescales.

Further to this, the boundary current is continually varying in response to changes in wind stress, with a mean acceleration for the period between 2015 and 2017. The time-dependent interior flow, combined with the increased roughness, may thus reduce the expected thickening of the bottom boundary layer, which may never reach arrest.

At the sill of OP we see hydrographic anomalies in temperature and density over 1,000 m from the bottom, however the down slope velocity anomalies are more tightly confined to the bottom 200 m. Whilst the scale of the hydrographic anomalies compares well to the changes in boundary layer thickness calculated along SSR, this layer thickness is likely an overestimate at the sill of OP. The vertical resolution of instrumentation (approximately every 100 m) in the mooring makes precise calculation of a bottom layer thickness difficult, as the changes expected are of similar magnitude to that of the spacing between the instruments. Calculating the vertical gradient of temperature and density and defining the thickness where the gradients significantly change from the interior shows changes in thickness of approximately 150 m. Whilst the gradient change between the two regimes is gradual this change occurs between 500 and 800 m above the slope.

Naveira Garabato et al. (2019) present results of detailed hydrographic surveys of the region finding near vertical isopycnals at the boundary with heights $\mathcal{O}(500m)$ consistent with the boundary layer thickness calculation from the moorings in the region. Polzin et al. (2014) also find boundary layers of $\mathcal{O}(500m)$ from Lowered Acoustic Doppler Current Profile measurements.

4.1.2. Adjustment Timescales

We can estimate how quickly the flow adjusts to the increased interior velocity diagnosed by the decreased lag times between OP2 and M2, by estimating the timescale for downslope Ekman transport to be arrested by buoyancy forcing. Garrett et al. (1993) find the arrest time to be proportional to the buoyancy frequency (N), frictional drag coefficient ($C_d = 2.5 \times 10^{-3}$), and Burger number ($s = 0.12$):

$$t_{arrest} = 0.5C_d^{-1}S^{-1.5}N^{-1}. \quad (2)$$

Using typical values for the northern boundary current region as for the boundary layer calculation above, we find $t_{arrest} = 54$ days. This timescale is consistent with the reduction in lag time between moorings, indicating an acceleration of the boundary current, and the reduction in transport found to be between 1 and 4 months from observations. Within OP, as before we observe $s \approx 1.3$, $N^2 \approx 3 \times 10^{-7}s^{-2}$. Using these values significantly reduces t_{arrest} to 5 days for the sill. This is likely to be an underestimate due to the assumption that layer growth is unimpeded. As found by Naveira Garabato et al. (2019), OP is a region of significant near boundary turbulence with instabilities acting to stratify the layer impeding the growth of the boundary layer.

The observed acceleration is also expected to cause a local barotropic spindown of the current. This is primarily due to friction with the boundary layer acting on the barotropic water column via Ekman processes communicating the bottom stress through the water column. Garrett et al. (1993) find this to be proportional to water column height (H), interior speed (U), and the drag coefficient:

$$t_{spin} = C_d^{-1} \left(\frac{H}{U} \right). \quad (3)$$

Using $H = 3000$ m, $U = 12$ cms^{-1} from the lagged cross correlation between M2 and OP2 and a typical value of $C_d = 2.5 \times 10^{-3}$ for the boundary current region, the spin-down time is approximately 150 days, three times longer than the response of the bottom Ekman layer. From this it is clear that the response of the bottom boundary layer dominates on timescales less than 5 months. Whilst the response within the boundary layer is initially dominant, the strong dependence on s and N will make a substantial difference to the layer's evolution and both boundary layer arrest and frictional spin down are linked and feedback off one another (Chapman, 2002). Further to this, a barotropic spin-down mechanism would cause changes in isopycnal height across the whole water column, thus changing the area of WSDW in OP. There is some evidence of full water column isopycnal displacement for the period from July 2015 onwards, when we see negative density anomalies across all depths in Figure 5.

4.2. Changes in AABW Formation

Variability in the volume and properties of bottom water formed within the Weddell Sea will superpose long-term changes on top of the observed variability in OP of northward IWSDW transport. Several of these mechanisms can themselves be triggered by changes in both local and gyre wide wind stress curl and wind stress (Darelius et al., 2016; Gordon et al., 2020; Jullion et al., 2013; McKee et al., 2011). Changes in AABW formation will cause a gyre wide shift in the depth of WSDW and WSBW within the water column, restricting the volume available to overflow the SSR. In general the timescale of formation changes is greater than the observed interannual changes in transport through OP due to the boundary layer mechanism, however sustained periods of anomalous wind forcing triggering these mechanisms, such as 2015–2017, makes attribution of IWSDW transport variability more challenging on longer timescales.

5. Conclusions

Using two sets of observational data acquired in the northern Weddell Sea, we have shown the occurrence of a synchronous warming and intensification of the abyssal boundary current carrying AABW into the Scotia Sea. These changes were concurrent with anomalously strong wind forcing within the Weddell Sea, and in particular around the SSR, the primary export pathway of this current. Using data from a mooring array in the deepest passage of the ridge, transport of IWSW is shown to have also decreased in response to the observed boundary current changes. Cross-correlation between the two moorings reveals the rapid timescale on which the boundary current responds to changes in forcing. This rapid response is indicative of a barotropic mechanism linking surface forcing to a reduction in AABW transport through OP.

The response of the bottom Ekman layer to changes in the interior flow speed, caused by a barotropic acceleration of the boundary current, is consistent with other observational data. This mechanism reduces the transport of the densest classes of AABW exported through the passage, warming and freshening the supply of AABW from the Weddell Sea. The evidence for this mechanism is limited by the constraints of observations in the passage; however, estimates of the timescales and changes in water mass area in the passage show this is the most plausible mechanism to explain the observed AABW transport changes on shorter timescales.

The changes in the wind strength and configuration shown to drive changes in AABW export through the passage are in part linked with modes of large-scale climate variability, such as the Southern Annular Mode (SAM) and the El Niño Southern Oscillation (ENSO) (Marshall, 2003). The intensity and frequency of these modes is predicted to increase as a result of anthropogenic forcing (Cai et al., 2022). If realized, the climate modes' increasing strength will drive stronger winds across the Weddell Sea, and will therefore be expected to cause further reduction in AABW export from the region, and stronger warming and freshening the bottom water supply. As such, understanding the mechanisms linking surface forcing to export is clearly of global importance. For example, AABW forms the bottom limb of the Atlantic Meridional Overturning Circulation, so any reduction in export may cause a slowdown in this system (Rintoul et al., 2001). Sustaining long-term observations of AABW export from the Weddell Sea will allow us to quantify and understand the variability of, and better constrain future changes in the overturning circulation.

Data Availability Statement

Mooring data from Orkney Passage used in the paper are available from the British Oceanographic Data Centre (BODC) at https://www.bodc.ac.uk/data/bodc_database/nodb/data_collection/6565/ (Abrahamsen, 2019). M2 mooring data used in the paper is available without restriction from <https://dods.ndbc.noaa.gov/thredds/catalog/data/oceansites/DATA/WDW/catalog.html>.

Wind stress data is from the ERA5 data set produced by Hersbach et al. (2020) and downloaded from the Copernicus Climate Change Service (C3S) (2023) (DOI: 10.24381/cds.f17050d7).

References

- Abrahamsen, E. P. (2019). Time series data collected from moorings deployed in the Orkney Passage (2007 onwards). [dataset]. British Oceanographic Data Centre. Retrieved from https://www.bodc.ac.uk/data/bodc_database/nodb/data_collection/6565/
- Abrahamsen, E. P., Meijers, A. J., Polzin, K. L., Naveira Garabato, A. C., King, B. A., Firing, Y. L., et al. (2019). Stabilization of dense Antarctic water supply to the Atlantic Ocean overturning circulation. *Nature Climate Change*, 9(10), 742–746. <https://doi.org/10.1038/s41558-019-0561-2>
- Armitage, T. W. K., Kwok, R., Thompson, A. F., & Cunningham, G. (2018). Dynamic topography and sea level anomalies of the southern ocean: Variability and teleconnections. *Journal of Geophysical Research: Oceans*, 123(1), 613–630. <https://doi.org/10.1002/2017JC013534>
- Brink, K. H., & Lentz, S. J. (2010). Buoyancy arrest and bottom Ekman transport. Part 1: Steady flow. *Journal of Physical Oceanography*, 40(4), 621–635. <https://doi.org/10.1175/2009JPO4266.1>
- Cai, W., Ng, B., Wang, G., Santoso, A., Wu, L., & Yang, K. (2022). Increased ENSO sea surface temperature variability under four IPCC emission scenarios. *Nature Climate Change*, 12(3), 228–231. <https://doi.org/10.1038/s41558-022-01282-z>
- Chapman, D. C. (2002). Deceleration of a finite-width, stratified current over a sloping bottom: Frictional spindown or buoyancy shutdown? *Journal of Physical Oceanography*, 32(1), 336–352. [https://doi.org/10.1175/1520-0485\(2002\)032<0336:DOAFWS>2.0.CO;2](https://doi.org/10.1175/1520-0485(2002)032<0336:DOAFWS>2.0.CO;2)
- Coles, V. J., McCartney, M. S., Olson, D. B., & Smethie, W. M. (1996). Changes in antarctic bottom water properties in the western South Atlantic in the late 1980s. *Journal of Geophysical Research C: Oceans*, 101(C4), 8957–8970. <https://doi.org/10.1029/95JC03721>
- Darelius, E., Fer, I., & Nicholls, K. W. (2016). Observed vulnerability of filchner-ronne ice shelf to wind-driven inflow of warm deep water. *Nature Communications*, 7(1), 12300. <https://doi.org/10.1038/ncomms12300>
- Fofonoff, N. P. (1957). Some properties of sea water influencing the formation of Antarctic bottom water. 1953. *Deep-Sea Research*, 4(C), 32–35. [https://doi.org/10.1016/0146-6313\(56\)90029-6](https://doi.org/10.1016/0146-6313(56)90029-6)

Acknowledgments

EFW, ACNG and CS were supported by the UK Natural Environment Research Council (NERC) Grant NE/K013181/1. EPA and MPM were supported by the UK Natural Environment Research Council (NERC) Grants NE/K012843/1 and NE/N018095/1. CDJA was supported by the INSPIRE Doctoral Training Partnership grant NE/S007210/1 project 2393716. ALG's work on the M2 mooring data work was supported by NOAA's Climate Program Office's Ocean Observing and Monitoring Division (Fund Ref 100007298). Lamont-Doherty Earth Observatory contribution number 8378. This research has received funding from the European Union's Horizon 2020 research and innovation program under grant agreement no. 821001.

- Foster, T. D., & Carmack, E. C. (1976). Temperature and salinity structure in the Weddell Sea. *Journal of Physical Oceanography*, 6(1), 36–44. [https://doi.org/10.1175/1520-0485\(1976\)006<0036:TASSIT>2.0.CO;2](https://doi.org/10.1175/1520-0485(1976)006<0036:TASSIT>2.0.CO;2)
- Garrett, C., MacCready, P., & Rhines, P. (1993). Boundary mixing and arrested ekman layers: Rotating stratified flow near a sloping boundary. *Annual Review of Fluid Mechanics*, 25(1), 291–323. <https://doi.org/10.1146/annurev.fl.25.010193.001451>
- Gill, A. E. (1973). Circulation and bottom water production in the Weddell Sea. *Deep-Sea Research and Oceanographic Abstracts*, 20(2), 111–140. [https://doi.org/10.1016/0011-7471\(73\)90048-X](https://doi.org/10.1016/0011-7471(73)90048-X)
- Gordon, A. L., Huber, B., McKee, D., & Visbeck, M. (2010). A seasonal cycle in the export of bottom water from the Weddell Sea. *Nature Geoscience*, 3(8), 551–556. <https://doi.org/10.1038/ngeo916>
- Gordon, A. L., Huber, B. A., & Abrahamsen, E. P. (2020). Interannual variability of the outflow of Weddell Sea Bottom water. *Geophysical Research Letters*, 47(4), e2020GL087014. <https://doi.org/10.1029/2020GL087014>
- Gordon, A. L., Huber, B. A., Hellmer, H. H., & Field, A. (1993). Deep and bottom water of the Weddell Sea's western rim. *Science*, 262(5130), 95–98. <https://doi.org/10.1126/science.262.5130.95>
- Grinsted, A., Moore, J. C., & Jevrejeva, S. (2004). Application of the cross wavelet transform and wavelet coherence to geophysical time series. *Nonlinear Processes in Geophysics*, 11(5/6), 561–566. <https://doi.org/10.5194/npg-11-561-2004>
- Hersbach, H., Bell, B., Berrisford, P., Hirahara, S., Horányi, A., Muñoz-Sabater, J., et al. (2020). The ERA5 global reanalysis. *Quarterly Journal of the Royal Meteorological Society*, 146(730), 1999–2049. <https://doi.org/10.1002/qj.3803>
- Jackett, D. R., & McDougall, T. J. (1997). A neutral density variable for the world's oceans. *Journal of Physical Oceanography*, 27(2), 237–263. [https://doi.org/10.1175/1520-0485\(1997\)027<0237:ANDVFT>2.0.CO;2](https://doi.org/10.1175/1520-0485(1997)027<0237:ANDVFT>2.0.CO;2)
- Johnson, G. C. (2008). Quantifying antarctic bottom water and north atlantic deep water volumes. *Journal of Geophysical Research*, 113(5), C05027. <https://doi.org/10.1029/2007JC004477>
- Jullion, L., Jones, S. C., Naveira Garabato, A. C., & Meredith, M. P. (2010). Wind-controlled export of antarctic bottom water from the Weddell Sea. *Geophysical Research Letters*, 37(9), L09609. <https://doi.org/10.1029/2010GL042822>
- Jullion, L., Naveira Garabato, A., Meredith, M. P., Holland, P. R., Courtois, P., & King, B. A. (2013). Decadal freshening of the antarctic bottom water exported from the Weddell Sea. *Journal of Climate*, 26(20), 8111–8125. <https://doi.org/10.1175/JCLI-D-12-00765.1>
- Jullion, L., Naveira Garabato, A. C., Bacon, S., Meredith, M. P., Brown, P. J., Torres-Valdés, S., et al. (2014). The contribution of the weddell gyre to the lower limb of the global overturning circulation. *Journal of Geophysical Research: Oceans*, 119(6), 3357–3377. <https://doi.org/10.1002/2013jc009725>
- Llanillo, P. J., Kanzow, T., Janout, M. A., & Rohardt, G. (2023). The deep-water plume in the northwestern weddell sea, Antarctica: Mean state, seasonal cycle and interannual variability influenced by climate modes. *Journal of Geophysical Research: Oceans*, 128(2). <https://doi.org/10.1029/2022jc019375>
- MacCready, P., & Rhines, P. (1993). Slippery bottom boundary layers on a slope. *Journal of Physical Oceanography*, 23(1), 5–22. [https://doi.org/10.1175/1520-0485\(1993\)023<0005:SBBLOA>2.0.CO;2](https://doi.org/10.1175/1520-0485(1993)023<0005:SBBLOA>2.0.CO;2)
- Marshall, G. J. (2003). Trends in the southern annular mode from observations and reanalyses. *Journal of Climate*, 16(24), 4134–4143. [https://doi.org/10.1175/1520-0442\(2003\)016<4134:TITSAM>2.0.CO;2](https://doi.org/10.1175/1520-0442(2003)016<4134:TITSAM>2.0.CO;2)
- Matano, R. P., Gordon, A. L., Muench, R. D., & Palma, E. D. (2002). A numerical study of the circulation in the northwestern Weddell Sea. *Deep-Sea Research Part II Topical Studies in Oceanography*, 49(21), 4827–4841. [https://doi.org/10.1016/S0967-0645\(02\)00161-3](https://doi.org/10.1016/S0967-0645(02)00161-3)
- McKee, D. C., Yuan, X., Gordon, A. L., Huber, B. A., & Dong, Z. (2011). Climate impact on interannual variability of Weddell Sea Bottom water. *Journal of Geophysical Research*, 116(5), C05020. <https://doi.org/10.1029/2010JC006484>
- Meijers, A., Meredith, M., Abrahamsen, E., Morales Maqueda, M., Jones, D., & Naveira Garabato, A. (2016). Journal of geophysical research: Oceans wind-driven export of Weddell Sea slope water. *Journal of Geophysical Research: Oceans*, 121(1900 m), 7530–7546. <https://doi.org/10.1002/2016jc011757>
- Meredith, M. P., Gordon, A. L., Naveira Garabato, A. C., Abrahamsen, E. P., Huber, B. A., Jullion, L., & Venables, H. J. (2011). Synchronous intensification and warming of antarctic bottom water outflow from the weddell gyre. *Geophysical Research Letters*, 38(3), L03603. <https://doi.org/10.1029/2010GL046265>
- Meredith, M. P., Naveira Garabato, A. C., Gordon, A. L., & Johnson, G. C. (2008). Evolution of the deep and bottom waters of the Scotia Sea, southern ocean during 1995–2005. *Journal of Climate*, 21(13), 3327–3343. <https://doi.org/10.1175/2007JCLI2238.1>
- Naveira Garabato, A. C. (2017). *Cruise report No. 47 RRS james clark ross cruise JRI6005 [cruise report]*. British Oceanographic Data Centre. Retrieved from https://www.bodc.ac.uk/resources/inventories/cruise_inventory/reports/jr16005.pdf
- Naveira Garabato, A. C., Frajka-Williams, E. E., Spingys, C. P., Legg, S., Polzin, K. L., Forryan, A., et al. (2019). Rapid mixing and exchange of deep-ocean waters in an abyssal boundary current. *Proceedings of the National Academy of Sciences of the United States of America*, 116(27), 13233–13238. <https://doi.org/10.1073/pnas.1904087116>
- Naveira Garabato, A. C., McDonagh, E. L., Stevens, D. P., Heywood, K. J., & Sanders, R. J. (2002). On the export of antarctic bottom water from the Weddell Sea. *Deep-Sea Research Part II Topical Studies in Oceanography*, 49(21), 4715–4742. [https://doi.org/10.1016/S0967-0645\(02\)00156-X](https://doi.org/10.1016/S0967-0645(02)00156-X)
- Naveira Garabato, A. C., Williams, A. P., & Bacon, S. (2014). The three-dimensional overturning circulation of the Southern Ocean during the WOCE era. *Progress in Oceanography*, 120, 41–78. <https://doi.org/10.1016/j.pocean.2013.07.018>
- Ohshima, K. I., Fukamachi, Y., Williams, G. D., Nishihashi, S., Roquet, F., Kitade, Y., et al. (2013). Antarctic Bottom Water production by intense sea-ice formation in the Cape Darnley polynya. *Nature Geoscience*, 6(3), 235–240. <https://doi.org/10.1038/ngeo1738>
- Orsi, A. H., Johnson, G. C., & Bullister, J. L. (1999). Circulation, mixing, and production of antarctic bottom water. *Progress in Oceanography*, 43(1), 55–109. [https://doi.org/10.1016/S0079-6611\(99\)00004-X](https://doi.org/10.1016/S0079-6611(99)00004-X)
- Polzin, K. L., Garabato, A. C. N., Abrahamsen, E. P., Jullion, L., & Meredith, M. P. (2014). Boundary mixing in Orkney passage outflow. *Journal of Geophysical Research: Oceans*, 119(12), 8627–8645. <https://doi.org/10.1002/2014JC010099>
- Purkey, S. G., & Johnson, G. C. (2010). Warming of global abyssal and deep Southern Ocean waters between the 1990s and 2000s: Contributions to global heat and sea level rise budgets. *Journal of Climate*, 23(23), 6336–6351. <https://doi.org/10.1175/2010JCLI3682.1>
- Purkey, S. G., & Johnson, G. C. (2012). Global contraction of antarctic bottom water between the 1980s and 2000s. *Journal of Climate*, 25(17), 5830–5844. <https://doi.org/10.1175/JCLI-D-11-00612.1>
- Purkey, S. G., & Johnson, G. C. (2013). Antarctic bottom water warming and freshening: Contributions to sea level rise, ocean freshwater budgets, and global heat gain. *Journal of Climate*, 26(16), 6105–6122. <https://doi.org/10.1175/jcli-d-12-00834.1>
- Rintoul, S. R., Hughes, C., & Olbers, D. (2001). *The antarctic circumpolar current system*. Academic Press.
- Spingys, C. P., Naveira Garabato, A. C., Legg, S., Polzin, K. L., Abrahamsen, E. P., Buckingham, C. E., et al. (2021). Mixing and transformation in a deep western boundary current: A case study. *Journal of Physical Oceanography*, 51(4), 1205–1222. <https://doi.org/10.1175/JPO-D-20-0132.1>

- Strass, V. H., Rohardt, G., Kanzow, T., Hoppema, M., & Boebel, O. (2020). Multidecadal warming and density loss in the deep Weddell Sea, Antarctica. *Journal of Climate*, *33*(22), 9863–9881. <https://doi.org/10.1175/JCLI-D-20-0271.1>
- Su, Z., Stewart, A. L., & Thompson, A. F. (2014). An idealized model of Weddell Gyre export variability. *Journal of Physical Oceanography*, *44*(6), 1671–1688. <https://doi.org/10.1175/JPO-D-13-0263.1>
- Thomson, R. E., & Emery, W. J. (2014). *Data analysis methods in physical oceanography* (3rd ed.). Elsevier Inc. <https://doi.org/10.1016/C2010-0-66362-0>
- Van Sebille, E., Spence, P., Mazloff, M. R., England, M. H., Rintoul, S. R., & Saenko, O. A. (2013). Abyssal connections of antarctic bottom water in a southern ocean state estimate. *Geophysical Research Letters*, *40*(10), 2177–2182. <https://doi.org/10.1002/grl.50483>
- Wang, Q., Danilov, S., Fahrbach, E., Schröter, J., & Jung, T. (2012). On the impact of wind forcing on the seasonal variability of Weddell Sea Bottom Water transport. *Geophysical Research Letters*, *39*(6). <https://doi.org/10.1029/2012GL051198>
- Zhou, S., Meijers, A. J. S., Meredith, M. P., Abrahamsen, E. P., Holland, P. R., Silvano, A., et al. (2023). Slowdown of antarctic bottom water export driven by climatic wind and sea ice changes. *Nature Climate Change*, *13*(7), 701–709. <https://doi.org/10.1038/s41558-023-01695-4>